Junction-Enhanced Polarization Sensitivity in Self-Powered Near-Infrared Photodetectors Based on Sb_2Se_3 Microbelt/ n-GaN Heterojunction

Peng Wan, Mingming Jiang,* Yun Wei, Tong Xu, Yang Liu, Sihao Xia, Longxing Su, Daning Shi, Xiaosheng Fang,* and Caixia Kan*

Polarization-sensitive photodetectors (PDs) based on anisotropic materials spark considerable interest for their potential applications in security surveillance, optical switches, and remote sensing. However, high-thickness or bulk anisotropic materials generally exhibit low polarization sensitivity, hindering their practical applications in polarization photodetection. Herein, a near-infrared (NIR) PD based on a p-type Sb_2Se_3 microbelt (MB)/n-GaN heterojunction is proposed. The Sb_2Se_3 MB/GaN PD effectively combines the anisotropy of the Sb_2Se_3 MB with the heterogeneous integration. The PD presents self-powered detection properties with a responsivity over 12 mA W^{-1}, a specific detectivity exceeding 5×10^{10} Jones, and a response speed (the rising/decaying times ≈74 ms/75 ms) under NIR illumination. More importantly, the heterojunction-based PD has a higher anisotropy ratio of 1.37, which is 1.3 times amplified as compared to the vertical photoconductive-type PDs (the anisotropy ratio of 1.06). The p-n junction's effect on carrier generation and recombination causes the increased polarization sensitivity of Sb_2Se_3 MB/GaN PDs, as confirmed by finite element method analysis. This work not only offers a deeper insight into polarization sensitivity regulated by junction or interface but also provides a practical method for developing high-sensitivity polarization detectors based on high-thickness or bulk anisotropic materials.

1. Introduction

Polarization-sensitive photodetectors (PDs) have drawn ever-increasing attention due to their detectable capability to the polarization states of light, whereas conventional PDs can only obtain the intensity and wavelength of the incident light.[1–3] They provide a new physical degree of freedom for modulating the photoelectric detection device and offer the potential for the improvement of detection accuracy and intelligence.[4,5] Applications for polarization-sensitive PDs include security surveillance, stress inspection, and target detection.[6,7] Conventional polarization-sensitive PDs are composed of a complex system with various optical sensors and coupling components, which presents a challenge for their miniaturization on a chip.[8] Low-dimensional anisotropic materials, especially 2D materials, provide an alternative method to address this issue for fabricating high-performance, low-cost, and miniature polarization PDs.[9] The strategy depending on the anisotropic optical properties, which are derived from the intrinsic anisotropic crystal structure, has been utilized to realize polarization sensitivity.[10,11] Many 2D anisotropic semiconductors, such as black phosphorus, SnS, ReS_2, $GeAs_2$, and In_2SnS_4, have been intensively investigated for their anisotropic structure and optoelectronic properties.[12–16] However, the transmission loss caused by the ultrathin active layer and insufficient light utilization still place restrictions on the photodetecting performance of the practical applications.[17,18] Although the incident light can be fully absorbed by increasing the thickness of anisotropic materials, the polarization sensitivity of PDs remarkably decreases.[2] Generally, anisotropic materials with a high thickness or bulk anisotropic materials show insufficient polarization sensitivity. Thus, finding an effective strategy to modulate the polarization-sensitive photoresponse of these materials is of scientific and technological significance, which is essential for industrial applications.

By engineering physical properties while maintaining the intrinsic nature of each component, homo/heterostructures provide a hint for overcoming this obstacle.[19–21] Great

P. Wan, M. Jiang, Y. Wei, T. Xu, Y. Liu, S. Xia, D. Shi, C. Kan
College of Physics
MIIT Key Laboratory of Aerospace Information Materials and Physics
Key Laboratory for Intelligent Nano Materials and Devices
Nanjing University of Aeronautics and Astronautics
Nanjing 211106, P. R. China
E-mail: mmjiang@nuaa.edu.cn; cxkan@nuaa.edu.cn
L. Su
School of Microelectronics
Southern University of Science and Technology
Shenzhen 518055, P. R. China
X. Fang
State Key Laboratory of Molecular Engineering of Polymers
Department of Materials Science
Fudan University
Shanghai 200433, P. R. China
E-mail: xshfang@fudan.edu.cn

**ADVANCED
SCIENCE NEWS**

www.advancedsciencenews.com

**ADVANCED
OPTICAL
MATERIALS**

www.advopticalmat.de

efforts have been made to fabricate PDs via the construction of p-n junctions and Schottky junctions by the photovoltaic effect.[22,23] Junction-based optoelectronic devices can separate photo-induced carriers by the built-in electric field at the junction interface and reduce the recombination in space, which offers excellent potential for advanced applications.[24–27] Recently, junction-based devices based on 2D anisotropic materials, such as black phosphorus p-n homojunction, GeAs/InSe, GeSe/MoS$_2$, and p-WSe$_2$/TaIrTe$_4$/n-MoS$_2$, have been proposed to develop polarization-sensitive PDs.[28–32] Even if high or enhanced polarization sensitivity has been observed in these junction-based polarization PDs, the impact of the junction on the polarization-sensitive activity of PDs and the internal physical mechanism deserves further study.[9]

In this work, we proposed and exhibited a kind of near-infrared (NIR) PDs based on a single p-type Sb$_2$Se$_3$ microbelt (MB)/n-GaN heterojunction for achieving polarization detection. High-quality Sb$_2$Se$_3$ MBs are prepared through a facile chemical vapor deposition (CVD) scheme. The asymmetry and anisotropic properties of individual Sb$_2$Se$_3$ MBs are characterized using angle-resolved polarized Raman spectroscopy and angle-resolved transmittance spectroscopy. The Sb$_2$Se$_3$ MB/GaN-based PD exhibits a high responsivity of 12 mA W^{-1}, a large specific detectivity of 5× 10^{10} Jones, and a fast response speed (the rise time of 74 ms and the decay time of 75 ms) upon NIR light irradiation in a self-biased mode. Importantly, the anisotropy ratio is as high as 1.37 under the 940 nm light illumination. Compared with Sb$_2$Se$_3$ MB-based vertical photoconductive PD, the anisotropy ratio is amplified 1.3 times. Based on the finite element method (FEM) analysis, the enhanced polarization sensitivity of the Sb$_2$Se$_3$ MB/n-GaN PD can be attributed to the p-n junction, which causes the difference between photo-induced carrier generation and recombination.

2. Results and Discussions

The Sb$_2$Se$_3$ crystals consist of chain-like [Sb$_4$Se$_6$]$_n$ ribbons along the [001] direction, which are extended by strong Sb—Se covalent bonds. Nevertheless, the ribbons stacked in the [100] and [010] directions are through weak van der Waals force (Figure S1, Supporting Information).[33] The chain-like structure indicates that Sb$_2$Se$_3$ tends to form 1D structures with [001] preferential growth orientation.[34,35] High-quality Sb$_2$Se$_3$ MBs were synthesized through a simple CVD method. The detailed synthesis process is available in Experimental Section and Figure S2, Supporting Information. **Figure 1**a displays the scanning electron microscopy (SEM) image of a representative Sb$_2$Se$_3$ MB. The wide top surface of Sb$_2$Se$_3$ MB is uniform and smooth, with a width of ≈100 µm. In addition, there are some fine and homogeneous stripes along the long axis at the edge of the Sb$_2$Se$_3$ MB. Energy-dispersive X-ray (EDX) spectroscopy was employed to identify the chemical composition of the Sb$_2$Se$_3$ MB. It can be observed that the Se and Sb elements are uniformly distributed throughout the Sb$_2$Se$_3$ MB and the chemical composition ratio of Se to Sb is 3 to 2 (Figure S3, Supporting Information). To further probe the crystallographic structure of the Sb$_2$Se$_3$ MB, high-resolution transmission electron microscopy (HRTEM) was carried out. As shown
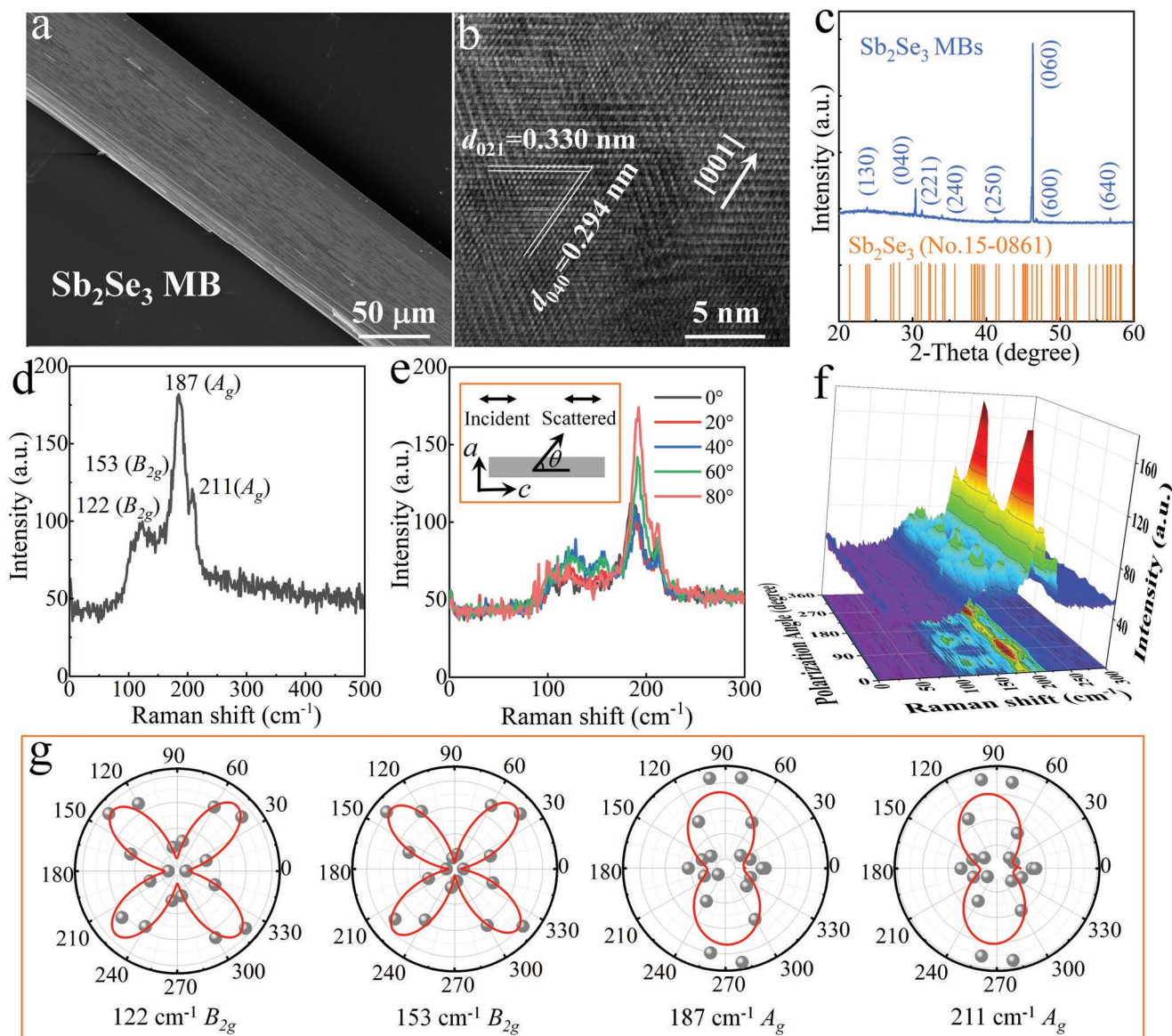
in Figure 1b, distinct lattice fringes can be observed. The interplanar distances are measured to be 0.330 and 0.294 nm, corresponding to the (021) and (040) planes, respectively. It suggests that the Sb$_2$Se$_3$ MB preferentially grows along the [001] direction.[36,37] The formation of Sb$_2$Se$_3$ MBs is well consistent with the general orientation of growth in nanostructures,[34,38] which is governed by the anisotropic nature of the building blocks.

The crystal structures of the Sb$_2$Se$_3$ MBs are confirmed by an X-ray diffractometer. As shown in Figure 1c, all diffraction peaks can be indexed to the orthorhombic phase of Sb$_2$Se$_3$ (JCPDS NO.15-0861) and no distinct impurity phases are observed.[39] It is worth noting that the intensities of (0k0) diffraction peaks are much higher than the conventional value, while the intensities of other reflection peaks are much lower, demonstrating that the wide top surface is the natural cleavage (010) plane.[40] The Sb$_2$Se$_3$ MBs were further evaluated with the assistance of unpolarized Raman spectroscopy. Figure 1d displays the Raman spectrum of a representative Sb$_2$Se$_3$ MB, which is measured at room temperature with a 532 nm laser excitation. Note that the high power density laser irradiation can cause the oxidization of Sb$_2$Se$_3$ into Sb$_2$O$_3$ in ambient air (Note S4, Supporting Information). Thus, the power intensity of the laser is kept low in Raman measurement.[41] Four characteristic Raman signal peaks are obtained at 122, 153, 187, and 211 cm^{-1}, respectively. The observed Raman peaks agree well with previous literature,[41,42] demonstrating that the high-quality Sb$_2$Se$_3$ MBs are prepared individually. Based on group theory analysis, Raman active modes of Sb$_2$Se$_3$ exhibit the following symmetries, $\Gamma = 10A_g + 5B_{1g} + 10B_{2g} + 5B_{3g}$.[8] A and B modes represent symmetric and anti-symmetric behavior, respectively. The subscript g reveals that the mode is symmetric under inversion. The Raman peaks at 122 and 153 cm^{-1} are corresponding to B_{2g} mode, while the Raman peaks at 187 and 211 cm^{-1} are attributed to A_g mode.[40]

Raman signal is highly sensitive to the crystal orientation owing to the optical transition selection rules.[4] Angle-resolved polarized Raman spectroscopy was employed to analyze the vibrational symmetries of the Sb$_2$Se$_3$ MB. The setup is depicted in the inset of Figure 1e. Rotatable linearly polarized light is perpendicularly incident on the top surface ((010) plane) of the Sb$_2$Se$_3$ MB. The polarization vector of scattered light is always parallel to the polarization vector of the incident light through a polarizer. The polarization angle (θ) is between the polarization vector and the c-axis of the Sb$_2$Se$_3$ MB. As shown in Figure 1e, different Raman mode intensities change with the variation of θ. Specifically, the Raman peaks at 122 and 153 cm^{-1} exhibit a period of 90°, while the Raman peaks at 187 and 211 cm^{-1} present a period of 180° (Figure 1f). To investigate the relationship between the polarized Raman signal and crystal axis more intuitively, the intensities of different Raman modes are extracted and plotted into polar graphs (Figure 1g). The polarized Raman intensity can be fitted via Raman tensor analysis in Note S5, Supporting Information.[18] The Raman scatter intensities (I) for A_g and B_{2g} modes are, respectively, expressed as

$$I_{A_g} \propto \left(A\sin^2\theta + C\cos^2\theta\right)^2 \qquad (1)$$

$$I_{B_{2g}} \propto \left(D\sin 2\theta\right)^2 \qquad (2)$$

ADVANCED
SCIENCE NEWS
www.advancedsciencenews.com

ADVANCED
OPTICAL
MATERIALS
www.advopticalmat.de

Figure 1. Morphology and characterizations of the Sb$_2$Se$_3$ MBs. a) SEM image of individual Sb$_2$Se$_3$ MB. b) HRTEM image of individual Sb$_2$Se$_3$ MB. c) XRD patterns of the Sb$_2$Se$_3$ MBs, where the JCPDS standard card (No.15-0861) of the Sb$_2$Se$_3$ is referenced. d) Unpolarized Raman spectroscopy of the Sb$_2$Se$_3$ MB. e) Angle-resolved polarized Raman spectroscopy of the Sb$_2$Se$_3$ MB as functions of the polarization angle (θ). The inset indicates that the polarization direction of the incident light is always parallel to that of the scattered light. The θ is between the polarization vector and the long axis (c-axis) of the Sb$_2$Se$_3$ MB. f) Polarized Raman intensity mapping of Sb$_2$Se$_3$ MB as functions of the wave number and the polarization angle. g) Polar plots of the Raman intensity of B_{2g} (122 cm^{-1}), B_{2g} (153 cm^{-1}), A_g (187 cm^{-1}), and A_g (211 cm^{-1}) modes, respectively.
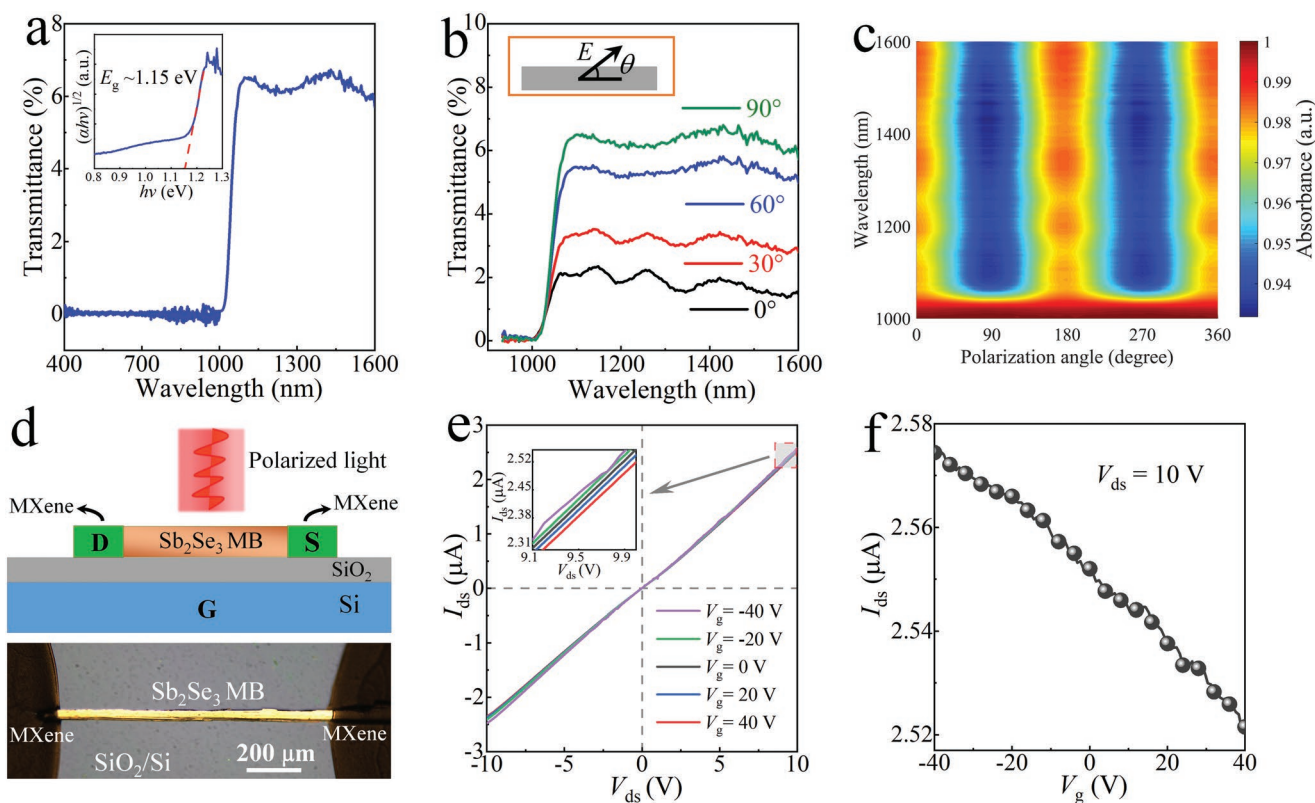
As shown in Figure 1g, the Raman intensities agree well with the theoretical prediction (Equations (1) and (2)). Furthermore, the c-axis (long axis) direction of the Sb$_2$Se$_3$ MB can be confirmed evidently based on the Raman tensor analysis. The characterization results suggest that high-quality Sb$_2$Se$_3$ MBs have been synthesized in this work, providing a foundation for the subsequent preparation of high-performance Sb$_2$Se$_3$ MB-based PDs.

To probe the optical properties of Sb$_2$Se$_3$ MBs, the transmission (T) spectra of a typical Sb$_2$Se$_3$ MB were measured. As shown in **Figure 2**a, there is no transmission light observed in the short wavelength region due to the high absorption

coefficient (α) and large thickness of Sb$_2$Se$_3$ MB. A sharp increase in transmission light occurs when the incident wavelength increases further. When the condition $\alpha d \approx 1$ is fulfilled, α can be calculated from $\alpha = -\ln(T)/d$.[43] According to Tauc's method, the optical bandgap of Sb$_2$Se$_3$ MB can be extracted using the following formula[44]

$$(\alpha h\nu)^\gamma = A(h\nu - E_g) \tag{3}$$

where $h\nu$ and A are the photon energy and the constant related to effective mass, respectively. γ is equal to 1/2 due to the indirect bandgap of the Sb$_2$Se$_3$.[43,45] As shown in the inset of

**ADVANCED
SCIENCE NEWS**

www.advancedsciencenews.com

**ADVANCED
OPTICAL
MATERIALS**

www.advopticalmat.de

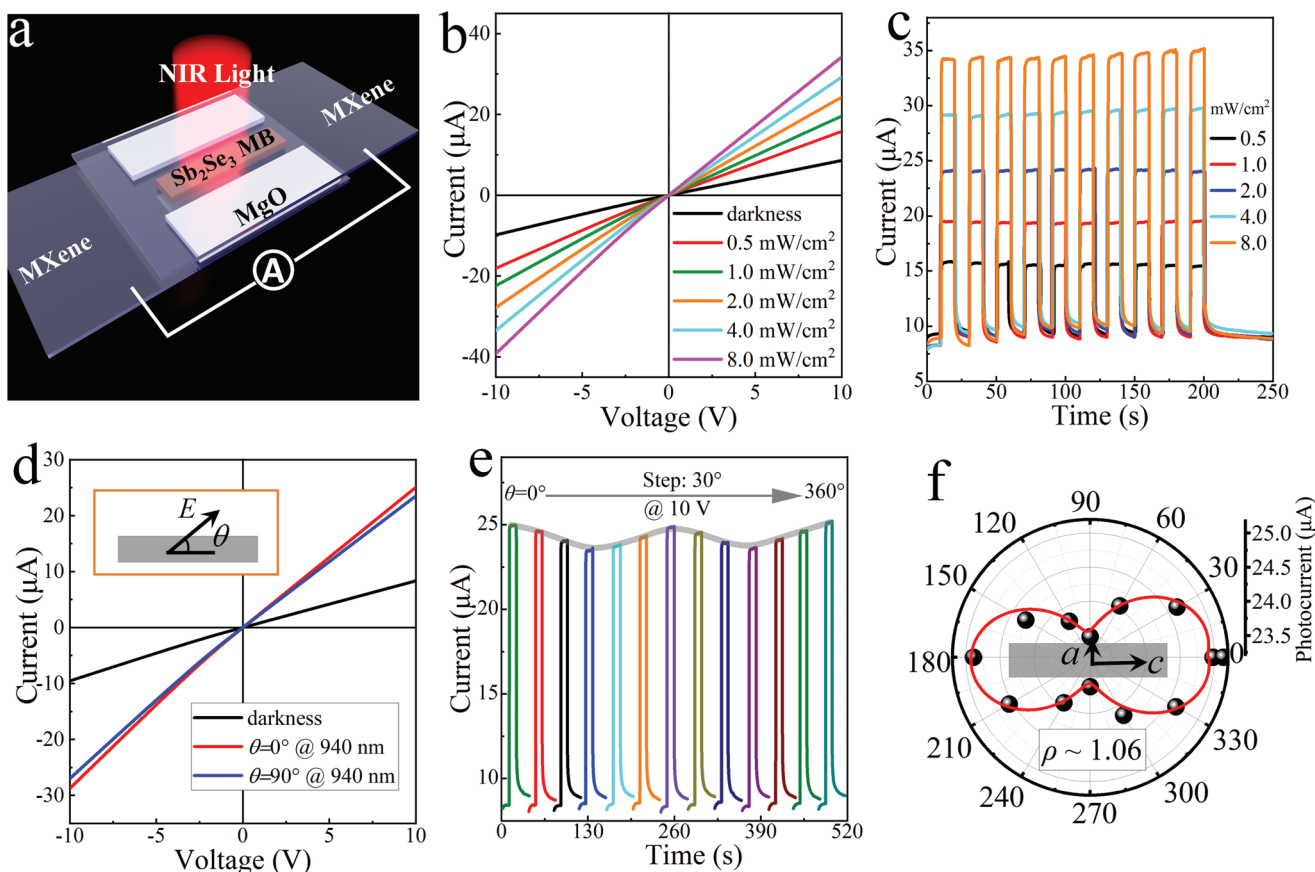**Figure 2.** Optical and electrical properties of the individual Sb_2Se_3 MB. a) Transmission spectra. The inset is $(\alpha h\nu)^{1/2}$ versus $h\nu$. b) Angle-resolved transmission spectra. The inset shows that the polarization angle (θ) is between the polarization vector and the long axis of Sb_2Se_3 MB. c) The corresponding 2D mapping of normalized absorption spectra as functions of the θ and the wavelength. d) Schematic diagram of a Sb_2Se_3 MB FET structure. The bottom is the optical micrograph of the Sb_2Se_3 MB FET. e) I_{ds}–V_{ds} characteristic curves of the Sb_2Se_3 MB FET at different V_g. The inset is the partially enlarged view of I_{ds}–V_{ds} curves. f) I_{ds}–V_g characteristic curve of the Sb_2Se_3 MB FET at a fixed V_{ds} of 10 V.

Figure 2a, the bandgap of Sb_2Se_3 MB is estimated as 1.15 eV, which is consistent with the previously reported literature (1.1–1.3 eV).[46,47]

Generally, the anisotropic structure of materials can contribute to dielectric, optical, and electrical anisotropy.[48] The angle-resolved transmission spectra of a Sb_2Se_3 MB were performed to investigate the optical anisotropy. As shown in Figure 2b, the intensity of transmitted light varies with the different polarization angles θ. The absorption can be normalized when the influence of polarization angle on reflection is neglected. As displayed in Figure 2c, the absorption exhibits a period of 180° in the long wavelength region ranging from 1050 to 1600 nm. The intensity of absorption presents maximum (minimum) values at $\theta = 0°$ ($\theta = 90°$). The absorption with the polarization vector parallel to the c-axis ($E//c$) is larger than the absorption with $E//a$, which indicates that the as-prepared Sb_2Se_3 MB exhibits obvious dichroism. The electrical properties of Sb_2Se_3 MBs were characterized by single MB-based field effect transistors (FETs). The schematic diagram of the Sb_2Se_3 MB FET structure is displayed in Figure 2d. Both the MXene films act as the source (S) and drain (D) electrodes. Si wafer serves as the back gate (G) electrode. The optical micrograph of a typical Sb_2Se_3 MB FET device is shown at the bottom of Figure 2d. The cross-sectional size of the Sb_2Se_3 MB was measured by the step profiler. The width and thickness of the Sb_2Se_3 MB are ≈37 and ≈27 µm, respectively (Figure S5, Supporting

Information). The distance between the source and drain electrodes is ≈980 µm. Figure 2e displays drain-source current (I_{ds}) versus drain-source voltage (V_{ds}) characteristic curves of the Sb_2Se_3 MB FET device at different gate voltages (V_g). At $V_g = 0$ V, the linear and symmetrical characteristic of the I_{ds}–V_{ds} curves indicates the Ohmic contact between Sb_2Se_3 MB and MXene. The I_{ds} increase with increasing V_{ds} and the slopes of the I_{ds} versus V_{ds} curves are dependent on the V_g (inset of Figure 2e). The I_{ds} versus V_g characteristic curve at a fixed V_{ds} of 10 V is shown in Figure 2f. The negative slope of the I_{ds} versus V_g curve demonstrates the p-type semiconducting transport behavior of the Sb_2Se_3 MB. Note that the Sb_2Se_3 MB channel could not be fully depleted due to the high conductance of Sb_2Se_3 MB and large channel length.[49] The mobility and carrier concentration are estimated as 0.14 $cm^2V^{-1}s^{-1}$ and 1.1×10^{17} cm^{-3}, respectively (the calculation method is described in Note S7, Supporting Information).

The MXene/Sb_2Se_3 MB/MXene PDs with vertical configuration were fabricated, in which the MXene conductive films serve as electrodes (**Figure 3**a). Note that the bilateral MgO insulating layer was designed to avoid direct contact between the MXene conductive electrodes. The NIR incident light ($\lambda = 940$ nm) was perpendicularly illuminated on the MXene/Sb_2Se_3 MB/MXene vertical PD. As shown in Figure 3b, the linear and symmetrical characteristic of the I–V curves under darkness indicates the Ohmic contact between Sb_2Se_3 MB and MXene for the vertical

**ADVANCED
SCIENCE NEWS**

www.advancedsciencenews.com

**ADVANCED
OPTICAL
MATERIALS**

www.advopticalmat.de

Figure 3. Photoresponse of the MXene/Sb$_2$Se$_3$ MB/MXene vertical PD. a) Schematic of the MXene/Sb$_2$Se$_3$ MB/MXene PD. b) I–V curves of the PD under darkness and 940 nm illumination with different power densities. c) I–T curves of the PD under 940 nm illumination with different power densities at a fixed voltage of 10 V. d) I–V characteristic curves of the PD under darkness and 940 nm polarized light illumination with a power density of 2 mW cm^{-2}. The inset shows that the polarization angle θ is between the polarization vector and the long axis of Sb$_2$Se$_3$ MB. e) I–T characteristic curves of the PD at a fixed voltage of 10 V with respect to the different θ. f) Corresponding polar plots of polarized photocurrent.
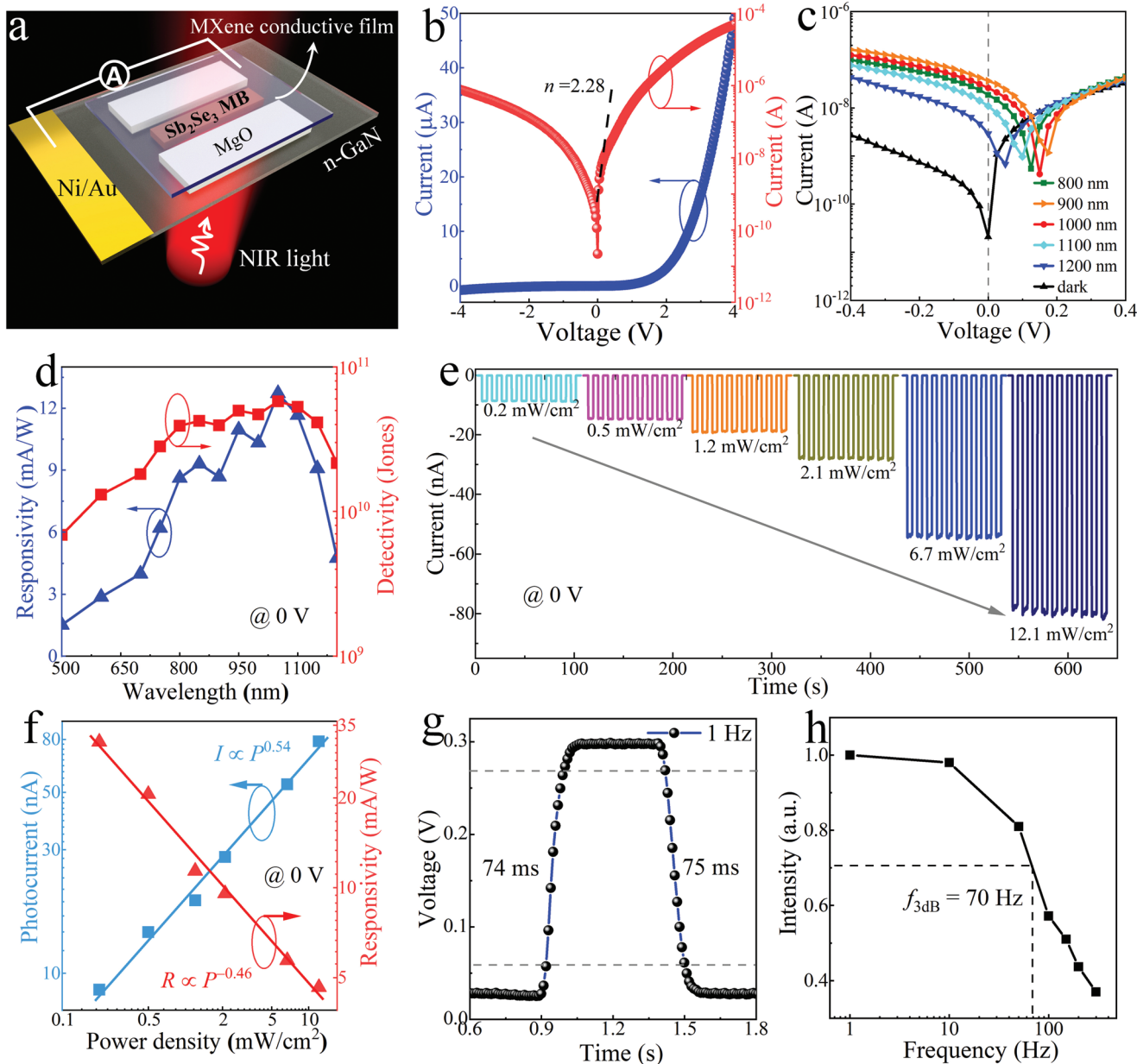
PD. In addition, the MXene/Sb$_2$Se$_3$ MB/MXene PD exhibits obvious NIR photoresponse. The photocurrent of the PD increases with the increase of the power density. As shown in Figure 3c, the photocurrents of the vertical PD vary immediately with repeatable switching characteristics at 10 V when the incident light switches between on and off.

The Sb$_2$Se$_3$ MBs exhibit intrinsic anisotropic optical properties, which indicates that the MXene/Sb$_2$Se$_3$ MB/MXene vertical PD can be applied to polarization-sensitive photodetection. The MXene/Sb$_2$Se$_3$ MB/MXene vertical PD is illuminated under 940 nm polarized light with a power density of 2 mW cm^{-2}. The polarization test system is shown in Note S8, Supporting Information, where the polarization angle θ is between the polarization vector and the long axis of Sb$_2$Se$_3$ MB. As shown in Figure 3d, the photocurrent ($\theta = 0°$) is larger than the photocurrent ($\theta = 90°$), indicating that the MXene/Sb$_2$Se$_3$ MB/MXene vertical PD presents polarization sensitivity. Figure 3e shows I–T characteristic curves of the PD at a fixed voltage of 10 V with respect to the different θ. The photocurrent exhibits a periodicity of 180° with the variation of θ. For clarity, the extracted photocurrent is plotted in Figure 3f, which is fitted by the following function[18]

$$I_{ph}(\theta) = I_{phmax} \cos^2 \theta + I_{phmin} \sin^2 \theta \tag{4}$$

where the I_{phmax} and I_{phmin} represent the maximum and minimum photocurrents, respectively. At the wavelength of 940 nm, a small anisotropic ratio ρ ($\rho = I_{phmax}/I_{phmin}$) is 1.06. Due to the large thickness of Sb$_2$Se$_3$ MB, the difference in actual absorption is small even if the absorption coefficient ($E//c$) is greatly larger than the absorption coefficient ($E//a$) in the NIR region.[50] The polarization sensitivity of the MXene/Sb$_2$Se$_3$ MB/MXene vertical PD does not achieve the desired results.

To investigate the influence of heterojunction structures on polarization photodetection, Sb$_2$Se$_3$ MB/n-GaN heterojunction PDs were fabricated. As shown in **Figure 4**a, the individual Sb$_2$Se$_3$ MB was transferred onto the n-GaN substrate with Ni/Au electrode acting as a cathode. Then the MXene conductive film was covered on the Sb$_2$Se$_3$ MB to serve as an anode. The NIR incident light was illuminated from the GaN side. The I–V characteristic curves in Figure 4b present a significant rectification behavior of Sb$_2$Se$_3$ MB/GaN heterojunction PD. In addition, the Sb$_2$Se$_3$ MB/GaN heterojunction PD yields a very low

ADVANCED
SCIENCE NEWS
www.advancedsciencenews.com

ADVANCED
OPTICAL
MATERIALS
www.advopticalmat.de

Figure 4. Photoresponse of the Sb$_2$Se$_3$ MB/GaN PD. a) Schematic of the Sb$_2$Se$_3$ MB/GaN PD. b) Logarithmic and linear I–V curves of the device under darkness. c) Logarithmic I–V curves of the device in dark and under illumination with different wavelengths. d) Wavelength-dependent responsivity and detectivity of the device under self-driven mode. e) I–T curves of the PD under 940 nm illumination with different power densities. f) Photocurrent and responsivity as functions of power densities. g) Photovoltage versus time at chopper frequency of 1 Hz extracted to evaluate the response speed. h) The normalized intensity of photovoltage as a function of the modulation frequency.

dark current of 20 pA under a bias voltage of 0 V. At low bias, the ideality factor (n) of a heterojunction can be obtained by[51]

$$n = \frac{e}{k_B T} \frac{dV}{d \ln I} \quad (5)$$

where e, k_B, and T are the elementary charge, the Boltzmann constant, and the temperature, respectively. The slope $d \ln I/dV$ at low voltage can be obtained from Figure 3b and the ideality factor is calculated to be 2.28. Based on the Sah–Noyce–Shockley theory, the ideality factor is close to one at the low

voltage.[23] The deviation of the ideality factor for the Sb$_2$Se$_3$ MB/GaN heterojunction may originate from the interface or surface recombination of electrons and holes.[52]

To examine the spectral response of the Sb$_2$Se$_3$ MB/GaN PD, the I–V curves of this device were measured under illumination with wavelengths ranging from 800 to 1200 nm (Figure 4c). The power density of the illumination at different wavelengths is shown in Figure S8, Supporting Information. The forward/backward I–V scan under darkness is performed to make sure there is negligible hysteresis near 0 V (Figure S9, Supporting Information). The Sb$_2$Se$_3$ MB/GaN PD shows a sensitive

photoresponse in the NIR region and can work at zero bias. To further examine the self-powered character of this device, $I–T$ curves of the Sb$_2$Se$_3$ MB/GaN PD were measured under illumination with different wavelengths (Figure S10, Supporting Information). Photocurrents of the Sb$_2$Se$_3$ MB/GaN PD vary immediately with repeatable switching characteristics under self-powered conditions as the incident light switches between on and off. Responsivity (R) of the Sb$_2$Se$_3$ MB/GaN PD can be determined by $R = (I_{ph}-I_d)/(PS)$, where I_{ph}, I_d, P, and S are the photocurrent, the dark current, the power density, and the effective cross-sectional area ($\approx 1.4 \times 10^{-3}$ cm^2), respectively.[9] As shown in Figure 4d, the Sb$_2$Se$_3$ MB/GaN PD shows a broad photoresponse. The maximum responsivity can reach 12 mA W^{-1} in the NIR region. With increasing the bias, the responsivity of the Sb$_2$Se$_3$ MB/GaN PD increases gradually (Figure S11, Supporting Information). The specific detectivity (D^*) usually describes the smallest detectable signal, which is limited mainly by three major noise sources, namely, flicker noise ($1/f$ noise), thermal noise, and shot noise from the dark current.[53] Considering the thermal noise ($i^2_{thermal} = 4k_BT / R_{shunt}\Delta f$) and shot noise ($i^2_{shot} = 2eI_d\Delta f$) for the PD without applied bias voltage, the detectivity can be expressed as[54,55]

$$D^* = R\sqrt{S\Delta f} \,/\, \sqrt{i^2_{thermal} + i^2_{shot}} = R\sqrt{S} \,/\, \sqrt{4k_BT / R_{shunt} + 2eI_d} \tag{6}$$

where Δf, R_{shunt}, and I_d are the bandwidth, the shunt resistance, and the dark current, respectively. R_{shunt} ($\approx 2.7 \times 10^8$ Ω) can be derived from the slopes of the $I–V$ curve under darkness (Figure 2b). The detectivity can reach up to 5×10^{10} Jones in the NIR region (Figure 4d), indicating that the Sb$_2$Se$_3$ MB/GaN PD can capture the signals of weak NIR irradiation at 0 V.
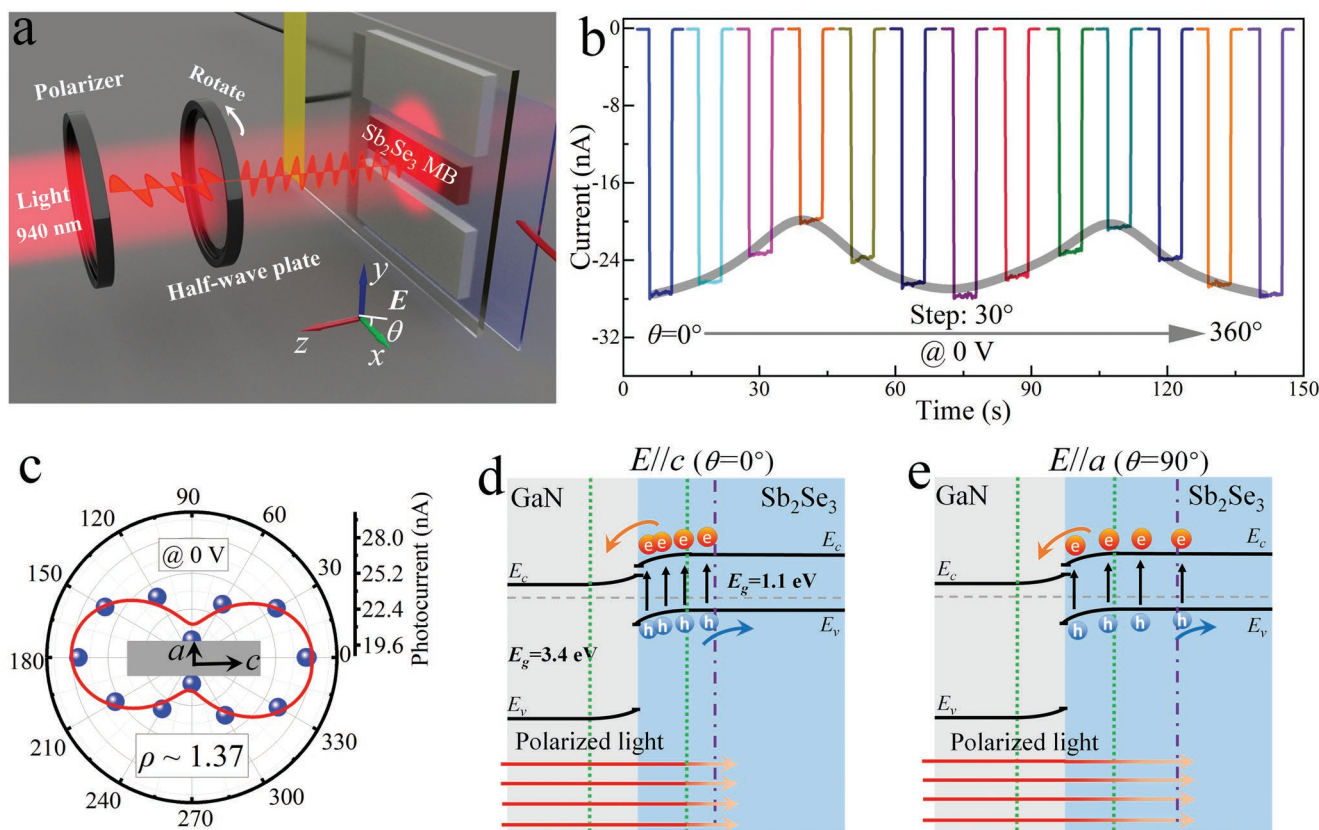
The photoresponse of the Sb$_2$Se$_3$ MB/GaN PD was further investigated under 940 nm illumination with different power densities. Figure 4e shows the $I–T$ curves of the PD under dark and illumination with various power densities. It can be clearly seen that the photoresponse of the PD increases with the increase of the power density. Moreover, the PD signal displays inconspicuous changes after several cycles, revealing that the PD has high stability and reproducibility. The photocurrent and responsivity of the PD under different power densities are plotted in Figure 4f. The power law ($I \propto P^\alpha$) is employed to fit the power density-dependent photocurrent, where α is the power-law factor.[56] The relationship between responsivity and power density can be described as $R \propto P^{1-\alpha}$. The α is calculated to be 0.54, which may be attributed to the large interface recombination of photogenerated carriers even under the conditions of low power-density light.[57] The response speed with rise time τ_{rise}= 60 ms and decay time τ_{decay}= 52 ms is estimated (Figure S12, Supporting Information), which is limited by the sampling rate of the semiconductor analysis device (Keysight B1500A). Thus, the response speed was further evaluated by an oscilloscope, in which a laser-driven light source (EQ-99X) combined with a monochromator and a chopper were used to stimulate the Sb$_2$Se$_3$ MB/GaN PD. The detailed test system is available in Note S14, Supporting Information. The photoresponse (photovoltage vs time) of the photodetector to NIR light with varied chopper frequencies of 1, 10, 50, and 100 Hz is shown in Figure S14, Supporting Information. At the low frequency, the photodetector exhibits distinct low and high photovoltage states.

The photovoltage degrades somewhat at a high frequency. The response time is calculated using the magnified photoresponse curve obtained at 1 Hz. As depicted in Figure 4g, the rise and fall times are deduced to be 74 and 75 ms, described by the time interval required for the photoresponse to increase/drop from 10%/90% to 90%/10% of its maximum value, respectively. The rise and fall times are comparable to the results measured by the semiconductor analysis device (B1500A), which indicates that the response speed of the photodetector is just at the limit of the semiconductor analysis device. The normalized intensity of photovoltage amplitude as a function of the modulation frequency is further investigated and plotted in Figure 4h. The intensity of photovoltage amplitude decreases with increasing modulation frequency. The 3 dB bandwidth that represents the frequency at which the photoresponse declines to 70.7% of its peak value has been determined to be 70 Hz.[58]

Furthermore, to investigate the polarization sensitivity of the Sb$_2$Se$_3$ MB/GaN PD, the NIR light ($\lambda = 940$ nm) was set to pass through a polarizer and an achromatic half-wave plate (**Figure 5**a). The partial-polarization light was converted to a linear polarization light and then the linear polarization direction was rotated by the half-wave plate. By changing the polarization direction and switching the on–off state of the light, the dynamic photoresponse of the Sb$_2$Se$_3$ MB/GaN PD was recorded. As shown in Figure 5b, the recorded photocurrent presents periodic changes with a maximum (minimum) value along the c-axis (a-axis) of the Sb$_2$Se$_3$ MB. The extracted photocurrent plotted intuitively in Figure 5c, which is fitted by Equation (4), demonstrates a good polarization sensitivity of the Sb$_2$Se$_3$ MB/GaN PD. Strikingly, a higher anisotropy ratio ($\rho = 1.37$) is achieved in Sb$_2$Se$_3$ MB/GaN heterojunction PD compared with the single Sb$_2$Se$_3$ MB-based vertical PD. Another eight Sb$_2$Se$_3$ MB-based vertical PDs and eight Sb$_2$Se$_3$ MB/GaN heterojunction PDs were fabricated by the method mentioned above. The polarization sensitivity was measured, as shown in Figure S15, Supporting Information. These results indicate that the existence of an as-formed heterojunction increases the polarization sensitivity of the devices based on anisotropic materials. To verify the self-powered operating mechanism of the Sb$_2$Se$_3$ MB/GaN heterojunction PD, energy band diagrams are shown in Figure 5d. The parameters of GaN and Sb$_2$Se$_3$, such as electron affinity and bandgap, are available in Table S1, Supporting Information. When the n-GaN contacts Sb$_2$Se$_3$ MB, electrons flow from the GaN side into the Sb$_2$Se$_3$ side to achieve thermal equilibrium owing to the high Fermi level of n-GaN. A space charge region and built-in electric field will be formed at the interface between the n-GaN and Sb$_2$Se$_3$ MB. When the Sb$_2$Se$_3$ MB/GaN heterojunction PD is illuminated by NIR light, the photons are absorbed and the electron holes are generated in the Sb$_2$Se$_3$ MB side. The photo-induced carriers can be separated by a built-in electric field to form a photocurrent without external bias.

To investigate the mechanism of the improved anisotropy ratio in the Sb$_2$Se$_3$ MB/GaN PD, the theoretical depletion width (d_p) in Sb$_2$Se$_3$ MB is calculated by the following function[59]

$$d_p = \sqrt{\frac{2\varepsilon_n\varepsilon_p\varepsilon_0 N_d V_{in}}{eN_a(\varepsilon_n N_d + \varepsilon_p N_a)}} \tag{7}$$

**ADVANCED
SCIENCE NEWS**

www.advancedsciencenews.com

**ADVANCED
OPTICAL
MATERIALS**

www.advopticalmat.de

Figure 5. Polarization sensitivity of the Sb$_2$Se$_3$ MB/GaN PD. a) Schematic representation of the polarization-sensitive Sb$_2$Se$_3$ MB/GaN PD. The polarization angle θ is between the polarization vector and the *x*-axis (the *c*-axis of the Sb$_2$Se$_3$ MB). b) Time-resolved photoresponse with the θ ranging from 0° to 360° under 940 nm illumination with a power density of 2 mW cm^{-2}. c) Corresponding polar plots of the polarized photocurrent at different θ. d) Energy band diagrams of the Sb$_2$Se$_3$ MB/GaN PD. For the polarization vector parallel to the *c*-axis of the Sb$_2$Se$_3$ MB ($E//c$, $\theta = 0°$), photo-induced electrons and holes are excited and separated partially in the depletion region. The green dotted line and purple dash-dotted line represent the boundary of the depletion layer and the optical penetration depth, respectively. e) Energy band diagrams of the Sb$_2$Se$_3$ MB/GaN PD. For $E//a$ ($\theta = 90°$), more photoinduced electrons and holes are excited and separated outside the depletion region.

where ε_n and ε_p are relative dielectric constants of GaN and Sb$_2$Se$_3$, respectively. N_d and N_a are carrier concentrations of GaN and Sb$_2$Se$_3$ MB, respectively. V_{in}, ε_0, and *e* are the built-in voltage (≈0.42 V), the permittivity of vacuum, and the elementary charge, respectively. The d_p is calculated as ≈18 nm (the related calculation parameters are shown in Note S15, Supporting Information). According to the absorption coefficient (≈10^5 cm^{-1}) for $E//c$, the penetration depth is calculated to be ≈100 nm.[50] It indicates that the photoinduced electrons and holes are partially excited in the depletion region, as shown in Figure 5d. The built-in electric field in the depletion region can spatially separate carriers, significantly reducing the recombination rate, and thereby, forming a large photocurrent. However, due to the absorption coefficient for $E//a$ being smaller than that for $E//c$, the more photo-induced carrier will generate outside the depletion region (Figure 5e). These carriers slowly diffuse toward the depletion region and become less efficient in separation.[21] The presence of a large number of carriers outside the depletion layer leads to severe recombination, making the formed photocurrent lower under the condition of $E//c$. Thus, the existence of the p-n junction will cause the difference in photocurrent and enhance the polarization sensitivity of the Sb$_2$Se$_3$ MB/GaN heterojunction PD.

To further confirm that the existence of the p-n junction has an influence on the polarization sensitivity, the spatial distribution of the optical field and the photoelectric properties of the Sb$_2$Se$_3$/GaN heterojunction are investigated based on FEM analysis. The detailed simulation method is available in Experimental Section. As shown in **Figure 6**a, the electric field of the incident light decreases gradually on the Sb$_2$Se$_3$ side due to the absorption. The electric field decays faster under the conditions of $E//c$, which results from the large absorption coefficient for $E//c$. The corresponding electric field intensity ($|E|$) with respect to the thickness of the GaN and Sb$_2$Se$_3$ is shown in Figure 6b. The penetration depth (*W*) for $E//c$ and $E//a$ is estimated as ≈100 and ≈200 nm on the Sb$_2$Se$_3$ side, respectively. The carrier spatial distribution of Sb$_2$Se$_3$/GaN heterojunction in the equilibrium state is shown in Figure 6c. It can be observed that the electron concentration (*n*) and hole concentration (*p*) are very low at the interface between GaN and Sb$_2$Se$_3$ due to the existence of a built-in electric field. The depletion width on the Sb$_2$Se$_3$ side is consistent with the calculation result based on Equation (6). In addition, the simulated energy band diagrams of the Sb$_2$Se$_3$ MB/GaN PD (Figure S16a, Supporting Information) are consistent with Figure 5d,e. The simulated photocurrent density (*J*) as a function of bias voltage (*V*) in
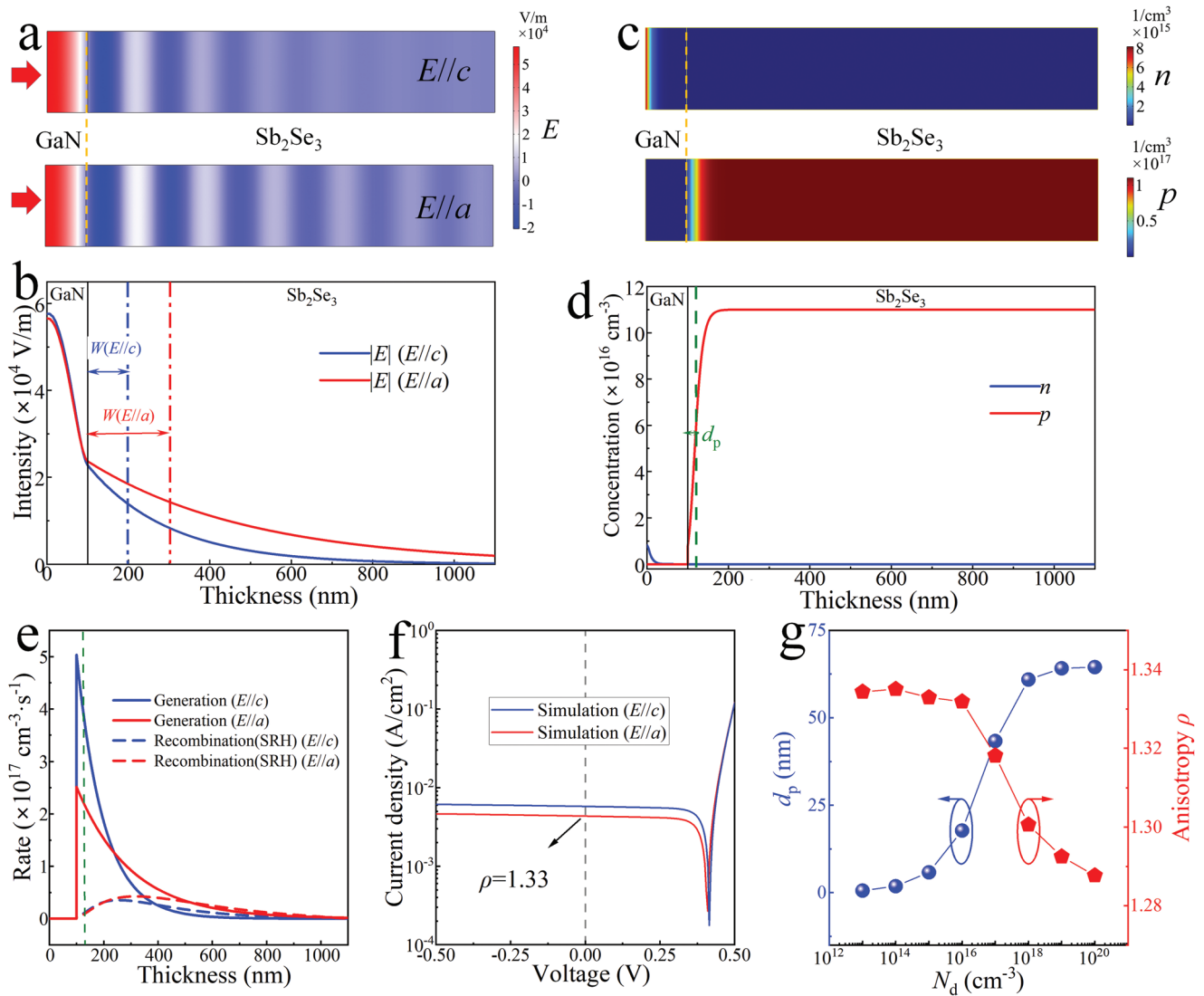
Figure 6. The simulation of Sb$_2$Se$_3$/GaN heterojunction based on FEM analysis. a) The electric field distributions in the Sb$_2$Se$_3$/GaN heterojunction, where the polarization vector of incident light is parallel to the c-axis ($E//c$) or a-axis ($E//a$) of Sb$_2$Se$_3$. b) The $|E|$ with respect to the thickness of GaN and Sb$_2$Se$_3$. c) The spatial distribution of n and p in the equilibrium state. d) The n and p with respect to the thickness of GaN and Sb$_2$Se$_3$ in the equilibrium state. The green dashed line is the theoretical depletion width (d_p). e) The generation and recombination rate of the Sb$_2$Se$_3$ MB/GaN heterojunction with respect to the thickness of GaN and Sb$_2$Se$_3$. The green dashed line is the theoretical depletion width (d_p). f) The simulated J–V curves of the Sb$_2$Se$_3$/GaN heterojunction under conditions of $E//c$ and $E//a$. g) The simulated d_p and ρ as functions of the doping concentration of n-GaN (N_d).

Figure S16b, Supporting Information, exhibits excellent rectification characteristics. These results confirm the formation of Sb$_2$Se$_3$/GaN heterojunction in simulation.

When the Sb$_2$Se$_3$/GaN heterojunction is radiated by NIR light, the photoinduced carrier generation occurs. The integral expression for the photoinduced carrier generation rate is described as[60]

$$G(x) = \int_\lambda \alpha(\lambda) \frac{\lambda}{hc} F(\lambda) \exp(-\alpha(\lambda)x) d\lambda \qquad (8)$$

where x is the depth into the Sb$_2$Se$_3$ from the interface, λ is the wavelength, $\alpha(\lambda)$ is the absorption coefficient, h is the Planck constant, c is the light speed, and $F(\lambda)$ is the spectral

irradiance. For simplicity, the incident light is regarded as monochromatic light (the wavelength is 940 nm) and $F(\lambda)$ is set as 1 mW cm^{-2}. Shockley–Read–Hall (SRH) recombination feature is added to capture the main recombination effect.[60] As shown in Figure 6e, the photoinduced carrier generation for $E//c$ mainly concentrates on the interface of Sb$_2$Se$_3$, whereas the spatial distribution of the photoinduced carrier generation for $E//a$ is wider. The recombination of carriers occurs in very few of the depletion regions and mainly takes place outside the depletion region. Thus, the difference in spatial distribution between carrier generation and recombination is expected to cause different photocurrents. The simulated J–V curves of the Sb$_2$Se$_3$ MB/GaN heterojunction under the illumination for $E//c$ and $E//a$ conditions are shown in Figure 6f. It can be observed

that the photocurrents under conditions of $E//c$ are larger than that under conditions of $E//a$. At zero bias voltage, the anisotropy is estimated as 1.33, which is close to the experimental results. The deviation may be attributed to the neglect of reflection and the simplification of carrier generation and recombination. With increasing the doping concentration (N_d) of GaN in simulation, the depletion width (d_p) in the Sb_2Se_3 side increases gradually and the calculated anisotropy (ρ) gradually decreases (Figure 6g). The result further supports that the existence of a p-n junction will cause the difference in photocurrent and modulate the polarization sensitivity of the Sb_2Se_3 MB/GaN heterojunction PD. In addition, the value of the absorption coefficients ($E//c$ and $E//a$) was adjusted in simulation and the anisotropy ratio of the Sb_2Se_3/GaN heterojunction PD was calculated (Figure S17, Supporting Information). The anisotropy ratio of the Sb_2Se_3/GaN heterojunction PD enhances by increasing the difference between the absorption coefficients ($E//c$) and the absorption coefficients ($E//a$). Thus, the polarization sensitivity of Sb_2Se_3 MB/n-GaN PD is achieved by combining the anisotropy of the Sb_2Se_3 materials with the p-n junction. It also demonstrates that if strongly anisotropic materials are selected to construct heterojunction-based PDs, higher polarization sensitivity can be obtained.

3. Conclusion

In this work, a self-powered PD based on a single high-quality Sb_2Se_3 MB/n-GaN heterojunction is constructed. The PD exhibits high performance with a responsivity of 12 mA W^{-1}, a specific detectivity of 5×10^{10} Jones, and a fast response speed (the rise time of 74 ms/the decay time of 75 ms) under self-powered conditions. By leveraging the anisotropy of the Sb_2Se_3 MB and the junction, the Sb_2Se_3 MB/n-GaN PD presents high polarization sensitivity. Compared with Sb_2Se_3 MB-based vertical PD, an amplified anisotropy ratio is up to 1.37. Based on the FEM analysis, the enhanced polarization sensitivity of Sb_2Se_3 MB/n-GaN PD originates from the p-n junction induced by the difference in spatial distribution between carrier generation and recombination. These findings help us to further clarify the polarization sensitivity modulated by the junction, which is of great significance to develop high-sensitivity self-powered polarization PDs based on the heterojunction or homojunction structure.

4. Experimental Section

Materials Preparation and Device Fabrication: The Sb_2Se_3 MBs were synthesized in a furnace tube through a CVD method. The high-purity Sb powder was loaded into a corundum boat and Si substrate was put on it. Then, the corundum boat was placed in the center of the furnace. Subsequently, another corundum boat full of high-purity Se powder was positioned upstream of the Sb powder. The weight ratio of Se to Sb was 3 to 2. The distance between the two precursors was 10 cm. During the growth process, the growth temperature was kept at 600 °C. A constant flow of argon (Ar, 150 sccm) served as the protective and carrier gas. Sb_2Se_3 MBs can grow onto the Si substrate by a chemical reaction of Se and Sb precursors. Quartz substrate was spin-coated with few-layered $Ti_3C_2T_x$ colloidal aqueous solution (5 mg mL^{-1}, Nanjing MKNANO Tech. Co., Ltd., www.mukenano.com) at 2000 r min^{-1} for 1 min, which

was followed by drying on a hot heating platform (80 °C) for 5 min. The spin coating and drying process were repeated five times to ensure the electrical conductivity of as-prepared MXene nanosheet films. The unintentionally-doped GaN wafer with a carrier concentration of 1×10^{16} cm^{-3} was cut into small pieces and was then cleaned. A bilateral MgO insulating layer ($\approx$1 µm) was deposited on a piece of as-prepared GaN film with a shadow mask by using electron beam evaporation. Ni/Au (30/100 nm) electrodes were deposited on GaN film using electron beam evaporation and subsequently followed by annealing. An individual Sb_2Se_3 MB was selected and then transferred in the slit of the as-prepared MgO insulating layer. A quartz substrate with MXene conductive films was tightly bonded with Sb_2Se_3 MB and acted as the top anode of the heterojunction device. The bilateral MgO insulating layer was designed to avoid direct contact between the MXene conductive electrode and the GaN film. Heterojunction-based PDs consisting of a p-type Sb_2Se_3 MB and an n-type GaN film were fabricated. MXene/Sb_2Se_3/MXene vertical photoconductive PDs were also fabricated. Single Sb_2Se_3 MB was picked out and transferred onto a SiO_2/Si substrate (Si: highly p-type doping, the thickness of $SiO_2 \approx$300 nm). Si wafer served as the back gate (G) electrode. The ends of single Sb_2Se_3 MB were applied by using MXene films. Both the MXene films acted as source (S) and drain (D) electrodes to fabricate a single MB-based FET.

Characterization and Measurements: The morphologies of the samples were characterized by SEM. The element distribution was conducted by using an EDX spectroscope. The X-ray diffraction (XRD) patterns of the samples were performed on an X-ray diffractometer equipped with Cu Kα radiation. The Raman spectra were analyzed by a micro-Raman spectrometer with a 532 nm laser serving as the excitation source. Angle-resolved polarization Raman spectra were acquired by rotating the polarization angle of the excitation laser with a half-wave plate. The polarization vector of the scattered light was parallel to the polarization of the incident light through a polarizer. Angle-resolved transmittance spectra of Sb_2Se_3 MBs were carried out through a polarization-dependent UV–infrared (UV–NIR) micro-absorption spectrum system (MStarter ABS). The photoelectric properties of the Sb_2Se_3 MB/GaN heterojunction PDs and FETs were measured by a characterization system including a semiconductor analysis device (Keysight B1500A) and a laser-driven light source (EQ-99X) combined with a monochromator. A power meter (Vega, Ophir) equipped with a thermal sensor (3A, Ophir) was carried out to calibrate the intensity of incident light. The fast response speed of the Sb_2Se_3 MB/GaN PD was measured by a system consisting of a laser-driven light source (EQ-99X) combined with a monochromator, a chopper, a resistance (10 GΩ), and a digital oscilloscope (Tektronix MSO54). The polarization sensitivity of PDs was measured by the system consisting of a NIR light-emitting diode (LED) (the wavelength is 940 nm), a collimating lens, a linear polarizer, a rotatable half-wave plate, and the semiconductor analysis device.

Simulation Methods: The electromagnetic distribution and photoelectric properties of the Sb_2Se_3/GaN heterojunction were investigated with FEM analysis using COMSOL Multiphysics software. A 2D electromagnetic simulation was performed on Sb_2Se_3/GaN heterojunction, where the NIR light (λ= 940 nm) was incident from the GaN side (the thickness d = 100 nm) to the Sb_2Se_3 side. The charge-depleting layer (d_p) and the penetration depth (W) in Sb_2Se_3 MB were far smaller than 1000 nm. The nonequilibrium carrier generation and recombination mainly occurred in and near the depletion layer. The thickness of the Sb_2Se_3 was set as 1000 nm in simulation, which was sufficient to simulate the influence of the junction on polarization sensitivity and address key issues. For simplicity, the absorption and the photo-generated carrier of GaN in the NIR region and reflection were neglected. The semiconductor module in software can calculate performance parameters of Sb_2Se_3/GaN heterojunction by the numerical solutions of the basic semiconductor equations. Because quantum size effects were not significant, the 2D model and semi-empirical method can be used in the simulation of Sb_2Se_3/GaN heterojunction. An n-type doping concentration of 1×10^{16} cm^{-3} for the GaN and a p-type doping concentration of 1.1×10^{17} cm^{-3} for the Sb_2Se_3. To illustrate the basic physics simply, the electrical contacts at the ends of the

device were assumed to be Ohmic contacts. The thermionic emission model determined the current transfer occurring between the different materials. To probe the photocurrent of Sb_2Se_3/GaN heterojunction under NIR irradiation, carrier generation and recombination were considered. The generation rate was defined according to different absorption coefficients under conditions of $E//c$ and $E//a$. The detailed simulation parameters for the Sb_2Se_3/GaN heterojunction are listed in Table S1, Supporting Information.

Supporting Information

Supporting Information is available from the Wiley Online Library or from the author.

Conflict of Interest

The authors declare no conflict of interest.

Data Availability Statement

The data that support the findings of this study are available in the supplementary material of this article.

[1] S. Chen, R. Cao, X. Chen, Q. Wu, Y. Zeng, S. Gao, Z. Guo, J. Zhao, M. Zhang, H. Zhang, *Adv. Mater. Interfaces* **2020**, *7*, 1902179.

[2] T. Wang, K. Zhao, P. Wang, W. Shen, H. Gao, Z. Qin, Y. Wang, C. Li, H. Deng, C. Hu, L. Jiang, H. Dong, Z. Wei, L. Li, W. Hu, *Adv. Mater.* **2022**, *34*, 2105665.

[3] D. Wu, M. Xu, L. Zeng, Z. Shi, Y. Tian, X. Li, C. Shan, J. Jie, *ACS Nano* **2022**, *16*, 5545.

[4] Y. Ping, H. Long, H. Liu, C. Chen, N. Zhang, H. Jing, J. Lu, Y. Zhao, Z. Yang, W. Li, F. Ma, X. S. Fang, Z. Wei, H. Xu, *Adv. Funct. Mater.* **2022**, *32*, 2111673.

[5] E. Zhang, P. Wang, Z. Li, H. Wang, C. Song, C. Huang, Z. G. Chen, L. Yang, K. Zhang, S. Lu, W. Wang, S. Liu, H. Fang, X. Zhou, H. Yan, J. Zou, X. Wan, P. Zhou, W. Hu, F. Xiu, *ACS Nano* **2016**, *10*, 8067.

[6] L. Tong, X. Huang, P. Wang, L. Ye, M. Peng, L. An, Q. Sun, Y. Zhang, G. Yang, Z. Li, F. Zhong, F. Wang, Y. Wang, M. Motlag, W. Wu, G. J. Cheng, W. Hu, *Nat. Commun.* **2020**, *11*, 2308.

[7] D. Tan, W. Zhang, X. Wang, S. Koirala, Y. Miyauchi, K. Matsuda, *Nanoscale* **2017**, *9*, 12425.

[8] S. Zhang, H. Wang, M. M. Kirchner, J. Liu, H. Luo, Y. Ren, C. Yuan, H. T. Hattori, A. E. Miroshnichenko, W. Lei, *Adv. Mater. Interfaces* **2022**, *9*, 2200448.

[9] J. Wang, C. Jiang, W. Li, X. Xiao, *Adv. Opt. Mater.* **2022**, *10*, 2102436.

[10] T. Yang, Y. Li, S. Han, Z. Xu, Y. Liu, X. Zhang, X. Liu, B. Teng, J. Luo, Z. Sun, *Small* **2020**, *16*, 1907020.

[11] L. Ye, P. Wang, W. Luo, F. Gong, L. Liao, T. Liu, L. Tong, J. Zang, J. Xu, W. Hu, *Nano Energy* **2017**, *37*, 53.

[12] J. Qiao, X. Kong, Z. X. Hu, F. Yang, W. Ji, *Nat. Commun.* **2014**, *5*, 4475.

[13] F. Liu, S. Zheng, X. He, A. Chaturvedi, J. He, W. L. Chow, T. R. Mion, X. Wang, J. Zhou, Q. Fu, H. J. Fan, B. K. Tay, L. Song, R. H. He, C. Kloc, P. M. Ajayan, Z. Liu, *Adv. Funct. Mater.* **2016**, *26*, 1169.

[14] Z. Zhou, M. Long, L. Pan, X. Wang, M. Zhong, M. Blei, J. Wang, J. Fang, S. Tongay, W. Hu, J. Li, Z. Wei, *ACS Nano* **2018**, *12*, 12416.

[15] Y. Cui, Z. Zhou, X. Wang, X. Wang, Z. Ren, L. Pan, J. Yang, *Nano Res.* **2021**, *14*, 2224.

[16] N. Zuo, A. Nie, C. Hu, W. Shen, B. Jin, X. Hu, Z. Liu, X. Zhou, T. Zhai, *Small* **2021**, *17*, 2008078.

[17] Q. Song, Y. Wang, F. Vogelbacher, Y. Zhan, D. Zhu, Y. Lan, W. Fang, Z. Zhang, L. Jiang, Y. Song, M. Li, *Adv. Energy Mater.* **2021**, *11*, 2100742.

[18] Q. Zhao, F. Gao, H. Chen, W. Gao, M. Xia, Y. Pan, H. Shi, S. Su, X. S. Fang, J. Li, *Mater. Horiz.* **2021**, *8*, 3113.

[19] C. Chen, K. Li, F. Li, B. Wu, P. Jiang, H. Wu, S. Lu, G. Tu, Z. Liu, J. Tang, *ACS Photonics* **2020**, *7*, 352.

[20] B. Ouyang, H. Zhao, Z. L. Wang, Y. Yang, *Nano Energy* **2020**, *68*, 104312.

[21] X. Zhang, L. Li, C. Ji, X. Liu, Q. Li, K. Zhang, Y. Peng, M. Hong, J. Luo, *Natl. Sci. Rev.* **2021**, *8*, nwab044.

[22] W. Song, J. Chen, Z. Li, X. S. Fang, *Adv. Mater.* **2021**, *33*, 2101059.

[23] M. Dai, H. Chen, R. Feng, W. Feng, Y. Hu, H. Yang, G. Liu, X. Chen, J. Zhang, C. Y. Xu, P. Hu, *ACS Nano* **2018**, *12*, 8739.

[24] K. S. Pasupuleti, M. Reddeppa, B. G. Park, K. R. Peta, J. E. Oh, S. G. Kim, M. D. Kim, *ACS Appl. Mater. Interfaces* **2020**, *12*, 54181.

[25] Y. H. Chen, L. X. Su, M. M. Jiang, X. S. Fang, *J. Mater. Sci. Technol.* **2022**, *105*, 259.

[26] D. Wu, C. Jia, F. Shi, L. Zeng, P. Lin, L. Dong, Z. Shi, Y. Tian, X. Lia, J. Jie, *J. Mater. Chem. A* **2020**, *8*, 3632.

[27] X. K. Li, X. G. Gao, B. W. Su, W. Xin, K. X. Huang, X. Q. Jiang, Z. B. Liu, J. G. Tian, *Adv. Mater.* **2018**, *5*, 1800960.

[28] H. Yuan, X. Liu, F. Afshinmanesh, W. Li, G. Xu, J. Sun, B. Lian, A. G. Curto, G. Ye, Y. Hikita, Z. Shen, S. C. Zhang, X. Chen, M. Brongersma, H. Y. Hwang, Y. Cui, *Nat. Nanotechnol.* **2015**, *10*, 707.

[29] J. Xiong, Y. Sun, L. Wu, W. Wang, W. Gao, N. Huo, J. Li, *Adv. Opt. Mater.* **2021**, *9*, 2101017.

[30] Y. Xin, X. Wang, Z. Chen, D. Weller, Y. Wang, L. Shi, X. Ma, C. Ding, W. Li, S. Guo, R. Liu, *ACS Appl. Mater. Interfaces* **2020**, *12*, 15406.

[31] X. Han, P. Wen, L. Zhang, W. Gao, H. Chen, F. Gao, S. Zhang, N. Huo, B. Zou, J. Li, *ACS Appl. Mater. Interfaces* **2021**, *13*, 61544.

[32] D. Wu, J. Guo, J. Du, C. Xia, L. Zeng, Y. Tian, Z. Shi, Y. Tian, X. Li, Y. Tsang, J. Jie, *ACS Nano* **2019**, *13*, 9907.

[33] N. Tideswell, F. Kruse, J. McCullough, *Acta Cryst.* **1957**, *10*, 99.

[34] M. Zhao, J. Su, Y. Zhao, P. Luo, F. Wang, W. Han, Y. Li, X. Zu, L. Qiao, T. Zhai, *Adv. Funct. Mater.* **2020**, *30*, 1909849.

[35] J. Wang, F. Guan, *CrystEngComm* **2020**, *22*, 68.

[36] D. Wang, D. Yu, M. Mo, X. Liu, Y. Qian, *J. Cryst. Growth* **2003**, *253*, 445.

[37] C. Zhao, X. Cao, X. Lan, *Mater. Lett.* **2007**, *61*, 5083.

[38] G. Y. Chen, B. Dneg, G. B. Cai, T. K. Zhang, W. F. Dong, W. X. Zhang, A. W. Xu, *J. Phys. Chem. C* **2008**, *112*, 672.

[39] G. Sun, B. Li, J. Li, Z. Zhang, H. Ma, P. Chen, B. Zhao, R. Wu, W. Dang, X. Yang, X. Tang, C. Dai, Z. Huang, Y. Liu, X. Duan, X. Duan, *Nano Res.* **2019**, *12*, 1139.

[40] N. Fleck, T. D. Hobson, C. N. Savory, J. Buckeridge, T. D. Veal, M. R. Correia, D. O. Scanlon, K. Durose, F. Jäckel, *J. Mater. Chem. A* **2020**, *8*, 8337.

[41] Z. Ma, S. Chai, Q. Feng, L. Li, X. Li, L. Huang, D. Liu, J. Sun, R. Jiang, T. Zhai, H. Xu, *Small* **2019**, *15*, 1805307.

[42] P. Vidal-Fuentes, M. Guc, X. Alcobe, T. Jawhari, M. Placidi, A. Pérez-Rodríguez, E. Saucedo, V. I. Roca, *2D Mater.* **2019**, *6*, 045054.

[43] C. Chen, W. Li, Y. Zhou, C. Chen, M. Luo, X. Liu, K. Zeng, B. Yang, C. Zhang, J. Han, J. Tang, *Appl. Phys. Lett.* **2015**, *107*, 043905.

[44] P. Wan, M. Jiang, T. Xu, Y. Liu, X. S. Fang, C. Kan, *Adv. Opt. Mater.* **2022**, *10*, 2101851.

[45] C. Chen, D. C. Bobela, Y. Yang, S. Lu, K. Zeng, C. Ge, B. Yang, L. Gao, Y. Zhao, M. C. Beard, J. Tang, *Front. Guided Wave Opt. Optoelectron.* **2017**, *10*, 18.

[46] R. Vadapoo, S. Krishnan, H. Yilmaz, C. Marin, *Phys. Status Solidi B* **2011**, *248*, 700.

[47] T. T. Ngo, S. Chavhan, I. Kosta, O. Miguel, H. J. Grande, R. Tena-Zaera, *ACS Appl. Mater. Interfaces* **2014**, *6*, 2836.

[48] Y. Yang, S. C. Liu, W. Yang, Z. Li, Y. Wang, X. Wang, S. Zhang, Y. Zhang, M. Long, G. Zhang, D. J. Xue, J. S. Hu, L. J. Wan, *J. Am. Chem. Soc.* **2018**, *140*, 4150.

[49] G. D. Yuan, W. J. Zhang, J. S. Jie, X. Fan, J. X. Tang, I. Shafiq, Z. Z. Ye, C. S. Lee, S. T. Lee, *Adv. Mater.* **2008**, *20*, 168.

[50] P. Wan, M. Jiang, L. Su, S. Xia, Y. Wei, T. Xu, Y. Liu, D. Shi, X. S. Fang, C. Kan, *Adv. Funct. Mater.* **2022**, *32*, 2207688.

[51] L. Zhang, P. Wan, T. Xu, C. Kan, M. Jiang, *Opt. Express* **2021**, *29*, 19202.

[52] D. Zhu, J. Xu, A. N. Noemaun, J. K. Kim, E. F. Schubert, M. H. Crawford, D. D. Koleske, *Appl. Phys. Lett.* **2009**, *94*, 081113.

[53] D. Zheng, H. Fang, P. Wang, W. Luo, F. Gong, J. C. Ho, X. Chen, W. Lu, L. Liao, J. Wang, *Adv. Funct. Mater.* **2016**, *26*, 7690.

[54] C. Bao, Z. Chen, Y. Fang, H. Wei, Y. Deng, X. Xiao, L. Li, J. Huang, *Adv. Mater.* **2017**, *29*, 1703209.

[55] Y. Hou, C. Wu, X. Huang, D. Yang, T. Ye, J. Yoon, R. Sriramdas, K. Wang, S. Priya, *Adv. Funct. Mater.* **2021**, *31*, 2007016.

[56] L. Wang, J. J. Li, Q. Fan, Z. F. Huang, Y. C. Lu, C. Xie, C. Y. Wu, L. B. Luo, *J. Mater. Chem. C* **2019**, *7*, 5019.

[57] L. Zeng, D. Wu, J. Jie, X. Ren, X. Hu, S. P. Lau, Y. Chai, Y. H. Tsang, *Adv. Mater.* **2020**, *32*, 2004412.

[58] M. Buscema, D. J. Groenendijk, S. I. Blanter, G. A. Steele, H. S. Van Der Zant, A. Castellanos-Gomez, *Nano Lett.* **2014**, *14*, 3347.

[59] L. Su, Q. Zhang, T. Wu, M. Chen, Y. Su, Y. Zhu, R. Xiang, X. Gui, Z. Tang, *Appl. Phys. Lett.* **2014**, *105*, 072106.

[60] A. Luque, S. Hegedus, *Handbook of Photovoltaic Science and Engineering*, Wiley, Sussex **2011**.

2202080 (12 of 12)